

Aero-Structural-Acoustic Gradient-based Optimization of Electric Ducted Fans

Judd Mehr^a, Tyler Critchfield^a, Eduardo J. Alvarez^b, Andrew Ning^a

^a*Brigham Young University, Provo, UT, 84604, USA*

^b*Whisper Aero, Crossville, TN, 38555, USA*

Abstract

There are many new and exciting technologies employing distributed electric propulsion, including applications for advanced air mobility (AAM). An important consideration for many AAM applications is the trade between aerodynamic performance and noise generation. Electric ducted fans (EDF) have been suggested as potentially able to meet both performance and noise generation constraints. In this work, we utilize gradient-based optimization employing an axisymmetric ducted rotor aerodynamic model, linear cascade surrogate model, geometrically exact beam structural model, and analytically and empirically based acoustics models to explore aero-structural-acoustic trades for EDF preliminary design. We explore rotor count and duct length configurations while optimizing rotor blade and duct geometry for minimum energy expense across a range of tonal sound power level constraints.

Our aero-structural-acoustic optimizations of electric ducted fans show that for the low blade counts studied in this work tonal sound power level sources modeled in this work can be reduced by 10 dB for each additional blade with a 0.6-0.7% increase in energy cost for the flight missions explored. Similarly an increase in duct length equal to the rotor tip radius yields a nearly 40 dB reduction in tonal sound power level with an accompanying 4.8% rise in energy expense. For a given configuration, small changes in rotor and duct geometry can provide a 4 dB decrease in tonal sound power level with less than a 1% rise in energy requirements. This work represents a first step in gradient-based, mid-fidelity, aero-structural-acoustic optimization of electric ducted rotors and sets the stage for future development efforts.

Keywords: Electric Ducted Fans, Advanced Air Mobility, Multi-disciplinary Optimization, Gradient-based Optimization, Aero-structural-acoustics

1. Introduction

Recent advances related to distributed electric and hybrid-electric aircraft propulsion have sparked investigations into novel aircraft configurations enabling the use of currently under-utilized regional airport infrastructure. In addition, electric powered aircraft also exhibit potential in energy, operation, and maintenance savings, as well as decreases in operation noise [1]. In order to achieve mainstream status, however, new electric powered aircraft designs must prove to be economically advantageous, as well as demonstrate a sufficient reduction in noise to garner public support of increased local airport traffic. More than ever, new aircraft concepts are required to be efficient and quiet while meeting flight mission requirements, requiring more comprehensive multi-disciplinary coupling design efforts.

With novel design considerations enabled by electric propulsion systems, previously unconsidered design spaces are open for exploration. It is often beneficial to begin exploration with rapid trade studies covering as much of the design space as is reasonable. For example, Koppelberg et al. performed various trade studies concerning the acoustics of ducted fans for small aircraft [2]. They report various considerations for reducing noise generation, including 3D blade design, rotor and stator blade numbers, rotor diameter, and rotor and stator axial spacing. They also discuss the necessity of designing for aerodynamics and acoustics together, as acoustically advantageous designs often come with aerodynamic penalties. It should be noted that they do not include rotor structural models in their studies; and therefore they limit some of their design space explorations to avoid potentially infeasible designs.

Because of conflicting trades such as those presented by Koppelberg et al., multi-disciplinary optimization techniques can be a great aid to the intelligent exploration of the design space. For instance, looking at multiple aerodynamic aspects of ducted fans, Qing et al. performed kriging assisted gradient-free optimization for a ducted fan in hover. They used a surrogate model produced from axisymmetric RANS for the duct and a momentum source model for the rotor. They found that integrated optimization (including design variables for both the interior duct and the rotor geometry) produced superior performance results compared to cases isolating the duct and rotor optimizations [3]. Jaron et al. used an evolutionary-based opti-

mization method for the multi-objective, aeroacoustic optimization of the fan stage for a next-generation passenger aircraft propulsor [4]. They used high-fidelity RANS, FEA, and a RANS informed analytic model for the aerodynamics, structures, and acoustics, respectively. Like Koppelberg et al., they also note a trade-off between acoustics and aerodynamics, showing that a 0.4% decrease in aerodynamic efficiency could lead to a 5dB decrease in tonal interaction noise and a 1.2dB increase in broadband noise. They also found that noise could be reduced with the right combination of rotor and stator blade numbers, showing that some low blade count designs had similar noise profiles to much higher blade count designs. Their interesting findings came at a cost, however: with 87 design variables, their gradient-free optimizations using high-fidelity models required roughly 12,000 configurations and roughly 2 million CPU-hours of computational time.

While gradient-free methods have been popular for multi-disciplinary optimization of various ducted rotor-based technologies (more examples include [5, 6]), gradient-based optimization methods may be preferred as design spaces increase in size due to their inherent scalability without much additional computation cost. For instance, Qiu used an adjoint-based quasi-Newton Broyden-Fletcher-Goldfarb-Shanno approach to the acoustic shape optimization of a duct inlet [7]. They were able to optimize the noise amplitude, leading to a shift in near-field sound propagation peak angle of 6 degrees without an appreciable effect on the aerodynamic performance of the duct inlet. Biava and Barakos also applied gradient-based techniques for the aerodynamic optimization of the duct shape and twist distribution of a ducted fan [8]. They found that they could improve the propulsive efficiency by 2 percent from baseline. Zhang and Barakos explored several gradient-based aerodynamic optimizations of ducted fans using adjoint enabled CFD methods [9]. They employed various combinations of duct inlet and outlet geometries and blade twist as design variables, but none of their optimizations included using all design variables simultaneously. They also performed interesting acoustic analysis in addition to their aerodynamic design optimizations and found that the duct itself had significant contributions to the sound signature.

For the most part, studies in the literature including gradient-based optimization of subsets of the aero-structural-acoustics of ducted fans tend to use high-fidelity methods such as RANS and 3D FEA. Even with the efficiency gained by employing gradient-based optimization techniques, high-fidelity tools can be computationally expensive. This computational cost may be

part of the reason why there are so few aero-structural-acoustic optimization studies in the literature. For preliminary design stages, computationally cheaper tools may be desired to help speed up initial explorations across larger portions of the design space. Thus for preliminary design exploration, mid-fidelity tools that make some simplifying assumptions compared to their high-fidelity counterparts are especially helpful. In early design stages, the reduction in fidelity becomes a worthwhile trade as cheaper tools allow for more rapid exploration of design spaces.

In this work, we seek to begin filling the gap of aero-structural-acoustic optimization in the literature by performing preliminary design optimization of EDF using aero-structural-acoustic, gradient-based optimization techniques. We employ mid-fidelity tools specifically designed for gradient-based optimization, including an axisymmetric ducted rotor aerodynamic model, geometrically exact beam structural model, and analytically and empirically based acoustics models. With the combination of purpose-built tools, we are able to perform rapid aero-structural-optimization with 12-18 design variables and more than 80 constraints across two application cases and several configurations to explore the aero-structural-acoustic trades in preliminary EDF design. This work represents a first step in gradient-based, mid-fidelity, aero-structural-acoustic optimization of electric ducted rotors and sets the stage for future development efforts.

The remainder of this paper is organized as follows: In section 2 we provide overviews of the aerodynamic, structural, and acoustic models used in this work, as well as information about how they are coupled. In sections 3 and 4 we explore two EDF design studies focused on aspects of the aerodynamic, structural, and acoustic considerations for EDF concepts. We then end in section 5 with concluding remarks.

2. Models

In this section, we overview the three major sets of models used in the multi-disciplinary optimizations presented in section 3, namely: aerodynamic, structural, and acoustic models. The aerodynamics are modeled using an axisymmetric, vortex-based method combining a panel method, actuator line, and axisymmetrically smeared wake model. The structures are modeled using a geometrically exact beam theory model. The acoustics are modeled using a unified analytic model based on the Goldstein acoustic analogy for tonal sound power level applied to an annular duct with center body.

The rest of this section provides overviews for each set of tools, and details on how they are coupled.

2.1. Aerodynamics

2.1.1. Ducted Rotor Aerodynamics

For aerodynamic analysis, we employ the Ducted Axisymmetric Propulsor Evaluation (DuctAPE) package, which is based on the ducted fan design code¹ and has been developed in the Julia [10] language specifically for use in gradient-based optimization [11, 12]. In this section, we cover the individual components contained within the DuctAPE code. Since the underlying theory for DuctAPE is discussed in previous work [11, 12], we will limit our discussion here to broad overviews of the methodology. As a general overview, also represented in fig. 1, DuctAPE combines an axisymmetric panel method to model the duct and center body, and an actuator line model combined with an axisymmetricly smeared wake model to model the rotor and wake.

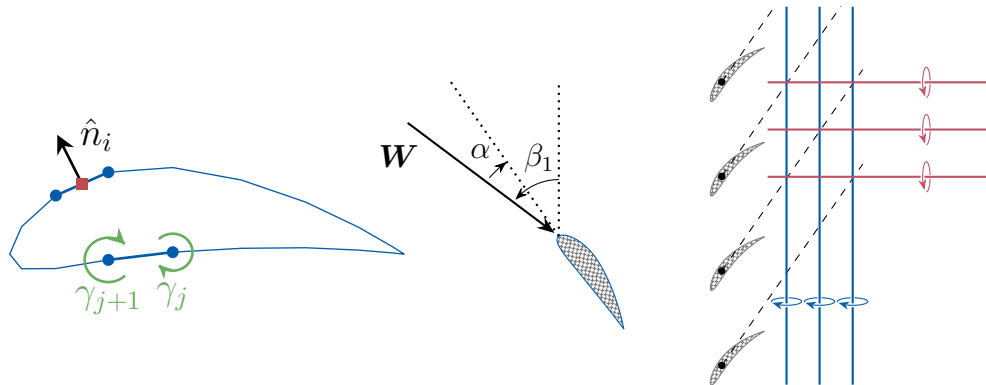


Figure 1: DuctAPE is composed of an axisymmetric panel method for duct bodies (left), an actuator line model for rotors (center), and smeared vortex filament model for wakes (right).

The duct and center body are modeled in DuctAPE using an axisymmetric linear vortex panel method. The panel method consists of assembling a linear system of equations to solve for the strengths of an unknown distribution of vortices along the body boundaries. The boundary condition used

¹<https://web.mit.edu/drela/Public/web/dfdc/>

in assembling the system of equations is the Neumann condition of no flow through panel control points.

$$\sum_{j=1}^N \gamma_j \mathbf{G}_{ij} = -(\mathbf{V}_\infty + \mathbf{V}_{\text{ext}}) \cdot \hat{\mathbf{n}}_i \quad (1)$$

where \mathbf{G} is comprised of the induced velocity normal to the i th control point due to the j th panel node, and γ_j is the strength of the linear vortex distribution associated with the j th panel node. \mathbf{V}_∞ is the freestream velocity (comprised only of the axial component in the axisymmetric case), and \mathbf{V}_{ext} are the externally induced velocities, namely the velocities induced by the rotor and wake.

Rotors are modeled in DuctAPE using an actuator and dragging line approach. Specifically, the body, wake, and rotor induced velocities are added together to calculate inflow angles and magnitudes at each blade element location and airfoil (or cascade) lookup tables are used to determine the section lift and drag (discussed in the next section). The blade section lift and drag determine the strengths of shed vortex filaments and source sheets placed on the blades, respectively.

The wake model in DuctAPE is an axisymmetrically smeared representation of the vortex filaments shed from the rotor blades. The axisymmetric vortex sheets are discretized into vortex panels like those used to model the duct and center body, with strengths dependent on the upstream rotor circulation and velocities induced on the wake. In turn the wake vortex panels induce velocities on the rotors and bodies, thereby coupling the wake to the rotors and bodies.

The body, rotor, and wake models are primarily coupled through mutually induced velocities, with the wake also being informed by the rotor circulation. The fully coupled non-linear system is solved for the set of velocities and vorticities fully characterizing the inviscid aerodynamics of the propulsor with a combination of a controlled successive over relaxation fixed-point method and a nested linear solve. As part of the post-process, we apply an integral boundary layer model to the duct to estimate viscous drag and penalize any separation that occurs. After post-processing, we are left with a variety of available outputs, including aerodynamic values of interest (for example: efficiency, thrust, torque, etc.) as well as aerodynamic loads that are used both in the structures and acoustics models that will be discussed shortly.

2.1.2. Rotor Blade Section Polars

For the optimizations in this work, we need to allow at least the thickness of the airfoil to change during the optimization to explore aero-structural trade-offs. If we could use constant airfoil sections, we could simply pre-compute the section aerodynamics which scale with chord length. As soon as we allow shape changes other than simple uniform scaling, however, we either need to include an airfoil analysis method directly into the optimization routine; or we need to augment our pre-computation approach into a more substantial surrogate model.



Figure 2: An isolated airfoil (left) differs from a linear cascade of airfoils (right) in that the airfoils in the cascade are influenced by the airfoils coming before and after (with decreasing influence out to infinity). The spacing between airfoils is determined by the blade section local solidity, and the skew of the cascade is determined by the stagger angle of the blade section.

In addition, the ducted fans as studied in this work require consideration of blade-to-blade aerodynamic interactions that are affected by local solidity and stagger angle. With blade-on-blade interactions prevalent, we cannot consider each blade element as an isolated airfoil as may be done in a typical open rotor case, but must treat it as a linear cascade of airfoils. As we can see in fig. 2, if we want to find the aerodynamic performance (specifically lift and drag) of an airfoil residing in a linear cascade, we need to take into account the surrounding airfoils, keeping in mind that the cascade extends to infinity in both directions. As the solidity increases, the airfoils in the cascade get closer together, and as the stagger angle of the blade section increases, the airfoils shift accordingly. Therefore we need some way to model the effects of changes in solidity and stagger on the linear cascade performance in addition to the nominal shape of the airfoil.

One such tool for viscous linear cascade analysis is MISES.² MISES cou-

²<https://web.mit.edu/drela/Public/web/mises/>

ples an Euler method and viscous boundary layer model applied with periodic boundary conditions to model viscous linear cascade aerodynamics. Unfortunately, like many legacy codes, MISES is not particularly robust nor does it provide sufficiently smooth outputs to be used directly in gradient-based optimization. Using MISES data, however, we can develop a surrogate model of the data that is sufficiently smooth and robust for gradient-based optimization.

There are many methods for developing surrogate models, but we found a straightforward approach using a combination of splines to be the most robust and accurate. We first use MISES to generate sets of lift and drag values across ranges of section thickness, solidity, stagger, and angle of attack. As the Reynolds numbers were generally consistent across the applications studied in this work, and we set Mach constraints as needed to keep the optimizer in check, we built our surrogate model with suitable constant values for Reynolds number ($2e6$) and Mach number (0.25). We then manually preprocess those lift and drag vs angle of attack polars to smooth them out by removing points due to non-physical noise. We then extend polars as needed by setting values after the maximum/minimum values constant to have consistent angles for each combination of section geometries. We then take the lift and drag polars for sets of solidity and stagger at single thickness values and fit 3D B-Spline surfaces to those sets of polars.

Since B-Spline surface fits for dimensions higher than 3D become inefficient to generate, in the optimizations we first sample each B-Spline surface based on the solidity and stagger for each blade element. We then apply an Akima spline interpolation [13] between the sampled surfaces based on the blade element thickness values for a given optimization iteration. This process gives us the appropriate lift and drag polars that we input into DuctAPE for the aerodynamic analysis of the ducted rotor system.

2.2. Structures

To model the structures of rotor blades, we approximate each rotor blade as a cantilever beam and apply geometrically exact beam theory (GEBT) [14, 15]. GEBT accurately captures nonlinear effects of highly flexible and slender beams, including finite displacements, and coupled bending-torsion-shear behavior. In this work, we use GXBeam.jl [16], a Julia package that enables efficient computation of exact automatic derivatives through the entire structural model and has been applied successfully to the structural analysis of rotors in gradient-based optimization applications [17, 18].

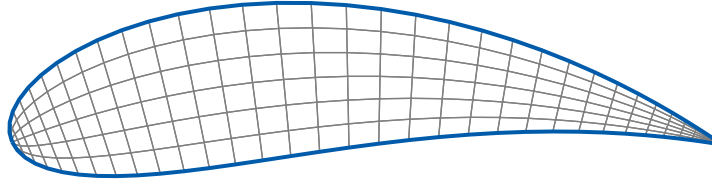


Figure 3: An example airfoil section showing the structural mesh (in gray) .

Perhaps the most vital inputs to GEBT methods are the stiffness and inertial properties of cross-sectional sections defined along the beam. We calculate these cross-sectional stiffness and inertial properties at each beam element’s center using a 2-D, finite element procedure [19] that uses bi-linear quadrilateral elements in the mesh (see fig. 3 for an example mesh). We selected a mesh refined to the point of less than 1% change in section structural parameters. Specifically, 35 elements in the x-direction and 6 elements in the y-direction as shown in fig. 3. Between each optimization iteration, the mesh node connection mapping is maintained as constant; and the mesh nodes are shifted smoothly according to airfoil thickness for a given iteration.

Table 1: Aluminum material properties used in this work.

E (GPa)	G (GPa)	ν	ρ (kg/m ³)	σ_c (MPa)	σ_t (MPa)	τ (MPa)
70	26	0.3	2700	275	275	200

For the optimizations in this work, we perform a set of steady-state structural analyses (one for each operating condition), where we fix the root section of the rotor blade in place and allow deflection along the rest of the blade. We use a beam reference frame that rotates around the rotor hub at a rate equal to that of the rotor rotation rate. We define the structural beam elements using the same set of radial locations we use to define the aerodynamic blade elements. Since the aerodynamic blade elements and structural beam elements are defined using the same set of coordinates, we apply aerodynamic forces from the aerodynamic model for each blade element directly to the corresponding beam elements as linearly varying distributed loads. For all rotor blades, we assume solid aluminum with material properties tabulated in table 1 where E is Young’s modulus, G is the shear modulus,

ν is Poisson's ratio, ρ is material density, σ is the tensile and compressive strength, and τ is the shear strength.

2.3. Acoustics

In this work, we use an in-duct noise propagation code developed at Whisper Aero that is designed for application in gradient-based optimization and contains decay of cut-off modes consistent with Tyler-Sofrin theory and a finite-length duct decay model. The code is based on the Goldstein acoustic analogy [20], which is a generalization of the Ffowcs Williams–Hawkings analogy [21] for an annular duct and center body. Note that for this work, we only model rotor tonal noise at the blade-passing frequency from thickness and loading aeroacoustic sources. Most of the implementation follows the unified formulation for predicting steady and unsteady sources of rotor/stator noise by Moreau [22] who also includes some validation of his models in his work. We provide a brief summary here. Specifically, the modal pressure can be described in terms of the modal amplitudes, A_{mn} :

$$p_m^\omega(z, r) = \sum_{n=0}^{+\infty} A_{mn}^\pm \frac{J_m(\kappa_{mn}^\nu \frac{r}{R_{\text{duct}}}) + Q_{mn} Y_m(\kappa_{mn}^\nu \frac{r}{R_{\text{duct}}})}{\sqrt{F_{mn}}} e^{ik_z^\pm z}, \quad (2)$$

where J_m and Y_m are the Bessel functions of the first and second kind of order m , respectively; k_z^\pm is the axial wave number (note the \pm superscript indicates direction of propagation with $+$ being downstream); ν is the hub-to-duct ratio $\nu \equiv \frac{R_{\text{hub}}}{R_{\text{duct}}}$; F_{mn} is a normalization factor; and κ_{mn}^ν and Q_{mn}^ν are the eigenvalue and coefficient, respectively, of the boundary-condition equation for concentric cylindrical walls.

Moreau developed an expression for the modal amplitudes derived from Goldstein's generalization of the Ffowcs Williams–Hawkings acoustic analogy:

$$A_{mn}^\pm = -i \sum_{b=1}^{N_B} \int_{R_{\text{hub}}}^{R_{\text{tip}}} \hat{g}_{mn}^\omega \cdot e^{-ik_z z_{LE} - im\Lambda_{LE}} \cdot \sigma dr_s, \quad (3)$$

and

$$\hat{g}_{mn}^\omega(r_s) = \frac{i}{4\pi R_{\text{duct}}} \frac{E_{mn}^\nu(r_s/R_{\text{duct}})}{k R_{\text{duct}} \alpha_{mn} \sqrt{F_{mn}}}; \quad (4)$$

and σ is the source strength of an arbitrary tonal noise component. Furthermore, Moreau, developed a unifying acoustic formulation in which all tonal sources (steady and unsteady) are expressed as

$$\sigma(r_s, \omega, \tilde{\omega}) = \underbrace{\mathcal{R}(r_s, \omega)}_{\text{acoustic radiation}} \cdot \underbrace{\Psi(r_s, \omega)}_{\text{chord-wise correlation}} \cdot \underbrace{\chi_0(r_s, \tilde{\omega})}_{\text{aerodynamic excitation}} \cdot \underbrace{e^{i\phi_0(r_s, \tilde{\omega})}}_{\text{phase of excitation}} ; \quad (5)$$

Table 2: Tonal noise sources included in this study.

Source	\mathcal{R}	Ψ	χ_0	ϕ_0
Thickness Terms	$k_\ell^2 c^2$	$\frac{1}{c} \int_{\ell=0}^c h_T(\ell) e^{-ik_\ell \ell} d\ell$	$\rho_0 W_0^2 \frac{\bar{t}}{c}$	0
Lift Loading Terms	$ik_n c$	$\frac{1}{c} \int_{\ell=0}^c h_L(\ell) e^{-ik_\ell \ell} d\ell$	$\frac{1}{2} \rho_0 W_0^2 C_L$	0

where in this work we model only rotor tonal noise at the blade-passing frequency from steady thickness and lift loading sources—with specific terms calculated as shown in table 2; where k_ℓ and k_n are the chord-wise and blade normal wave numbers, respectively; h_T and h_L are the thickness and loading distributions, respectively; c , \bar{t}/c , ρ_0 , W_0 , and C_L are the chord length, thickness to chord ratio, local density, local inflow velocity, and lift coefficient of the blade section, respectively.

2.4. Finite-Duct Model

As described by Moreau [22], the modal sound power Π_m^ω transmitted infinitely upstream (−) and downstream (+) of a duct is calculated as

$$\Pi_m^{\omega\pm} = \sum_{n=0}^{\infty} \pi R^2 \frac{|A_{mn}^\pm|^2}{\rho a} \alpha_{mn} C_{mn}^\pm T_{mn}, \quad (6)$$

where C_{mn}^\pm is called the modal convection factor and represents the energy amplification or attenuation due to flow convection, defined as

$$C_{mn}^\pm = \left(\frac{1 - M_x^2}{1 \mp \alpha_{mn} M_x} \right)^2, \quad (7)$$

and T_{mn} is the modal transmission coefficient defined as

$$T_{mn} = \frac{4\alpha_{mn}}{(1 + \alpha_{mn})^2}. \quad (8)$$

Moreau's expression for the modal sound power, $\Pi_m^{\omega\pm}$, applies only to the cut-on modes, which implicitly assumes an infinitely long duct along which all cut-off modes have decayed by the time they reach the inlet and exhaust. For this work, we have developed a model that captures the correct physical trends for the decay of the modal pressure to account for both cut-on and cut-off modes in a finite-length duct:

$$\Pi_m^{\omega\pm} = \sum_{n=0}^{\infty} \pi R^2 \frac{|A_{mn}^{\pm} \xi^{\pm}|^2}{\rho a} |\alpha_{mn}| C_{mn}^{\pm} T_{mn}, \quad (9)$$

where

$$\xi^{\pm} = e^{-\text{Im}(k_z^{\pm})z} e^{-\frac{\text{Im}(\alpha_{mn})^3}{(|k_z^{\pm}|^{1/4} + |\alpha_{mn}|^{1/2})^2}}, \quad (10)$$

$\text{Im}(k_z)$ denotes the imaginary part of the wave number, and z is the length of the duct from rotor to inlet or exhaust.

2.5. Model Coupling

The aerodynamics and structures are coupled with a simple one-way coupling in which aerodynamic loads are passed into the structural model. The structural model takes the same geometric information for blade sections as the aerodynamic model. Therefore the blade section geometries and aerodynamic loads are passed directly into the structural analysis. Similarly the aerodynamics and acoustics have a one-way coupling where acoustically relevant aerodynamic outputs (namely aerodynamic loads) are passed into the acoustics model along with acoustically relevant geometric details of the ducted fan. The acoustics and structures are not coupled; thus we assume that any structural vibrations are negligible relative to the modeled acoustics. In addition, since there is only a one-way coupling between the aerodynamics and structures, we assume small deflections which are constrained in the optimization as discussed in the next section.

3. Optimization Methods

For the optimizations in this work, we select an expended energy minimization problem that includes aerodynamics (both linear cascade blade section and ducted rotor), structures, and acoustic disciplines. The overall optimization problem is formulated as:

Minimize energy expenditure;
with respect to: duct geometry (3 variables), rotor geometry (6-12 variables),
rotor rotation rate (3 variables);
subject to: required thrusts,
maximum tonal sound power level,
maximum change in broadband overall sound pressure level,
structural failure,
maximum structural deflection,
minimum rotor section thickness;

where in total the problem size is 12-18 design variables with more than 80 constraints. We compare across two conventional takeoff and landing application cases: a generic small UAS, and a 2-seat trainer aircraft based on the Airbus E-Fan demonstrator. The major aircraft parameters used to define the objective and thrust constraints are shown in table 3.

To estimate the energy expenditure, E_{tot} , we take the rotor power, P , from each operating point (static, climb, cruise) and multiply them by the respective times, t , in each condition and then sum the resulting energies. We make some assumptions here, namely that the static thrust is constant during a conventional takeoff, climb happens at a constant velocity, and we neglect the decreased energy expense during approach and landing (thus assuming that the remaining mission time is spent in cruise rather than glide/descent, etc.). When calculating the power for climb, we also take a single operating point at an altitude half-way between sea level and the cruise altitude. We additionally assume the static condition takes place at sea level. Together we have

$$E_{tot} = P_s t_s + P_{cl} t_{cl} + P_{cr} t_{cr} \quad (11)$$

where the subscripts (st), (cl), and (cr) represent the static, climb and cruise operating points, respectively.

Table 3: Major vehicle parameters used for the optimizations in this work.

Parameter	Symbol	Units	UAS	2P
Number of Propulsors	N_p		1	2
Approximate Rotor Diameter		in	6	24
Nominal Takeoff Weight		lb	50	1200
Static Thrust to MTOW	$\left(\frac{T}{W}\right)_s$		0.35	0.35
Cruise Velocity	V_{cr}	mph	50	120
Climb Velocity	V_{cl}	mph	30	72
Cruise Lift/Drag	$\left(\frac{L}{D}\right)_{cr}$		12	15
Climb Lift/Drag	$\left(\frac{L}{D}\right)_{cl}$		10	12
Cruise Altitude	h_{cr}	ft	1500	5500
Climb Angle	γ_{cl}	degrees	5	5
Cruise Range	R_{cr}	mi	30	100

The various times (in seconds) for each operating condition are given by

$$\begin{aligned}
 t_s &= 10 \\
 t_{cl} &= \frac{h_{cr}}{V_{cl} \sin(\gamma_{cl})}, \\
 t_{cr} &= \frac{R_{cr}}{V_{cr}}.
 \end{aligned} \tag{12}$$

where h_{cr} is the cruise altitude, γ_{cl} is the climb angle, R_{cr} is the cruise range, and V_{cr} is the cruise velocity.

The thrust constraints for static, climb, and cruise conditions are defined based on the maximum takeoff weight, MTOW, to be

$$\text{Static Thrust} = \frac{\text{MTOW} \frac{T_s}{W}}{N_p}; \quad (13a)$$

$$\text{Climb Thrust} = \frac{\text{MTOW}}{N_p} \left[\frac{1}{\left(\frac{L}{D}\right)_{cl}} + \sin(\gamma_{cl}) \right]; \quad (13b)$$

$$\text{Cruise Thrust} = \frac{\text{MTOW}}{\left(\frac{L}{D}\right)_{cr} N_p}; \quad (13c)$$

where T_s/W is the static thrust to weight ratio, N_p is the number of propulsors, and L/D is the lift to drag ratio.

Note in table 3 that we set the nominal takeoff weight of the aircraft. For the thrust constraints, we add to that nominal weight the weight of the duct shroud and center body and the blade weight. The total weights of the duct bodies and rotor blades are not particularly large relative to the nominal vehicle weight; but as we will be changing duct and rotor geometries in these studies, the thrust requirements should be updated accordingly. We assume the motor weight stays constant and is included in the nominal vehicle weight. To determine the rotor weight, we simply take the mass of the blade as determined by the structural model, multiply by the number of blades, and multiply by gravity to obtain a weight. For the duct shroud and center body, we assume a 2 mm thick carbon fiber reinforced polymer shell structure and compute the surface area of the bodies, multiply by the thickness and density to approximate the mass, and then multiply by gravity to get a weight. We assume the composite shell to dominate any other possible weight contributors that would change with changing duct shape (such as internal foam, etc.).

3.1. Structural, Manufacturing, and Acoustic Constraints

For the rotor structural constraints, we constrain the rotor blade tip to deflect no more than 7 percent of the blade radius which corresponds to a tip gap of 0.25 percent of the rotor radius. We selected this level of allowable bending as the experiments used in validating DuctAPE had a rotor with a tip gap of 0.25 percent, and DuctAPE matched well in that case [12]. Therefore we would expect DuctAPE to be accurate within that margin. We also include failure constraints at the blade root and at various stations along the blade using a von Mises failure criterion implemented in our structural

model code. We also set a minimum chord length of $c_{min} \geq 0.05R_{tip}$ across the blade in order to aid the optimizer in finding structurally feasible solutions for which GXBeam will converge.

We set a manufacturing constraint of a minimum thickness of 2 mm at each section along the blade. Exploring potential manufacturing methods, we found 2 mm to be a reasonable cutoff after which significant increases in manufacturing cost and quality control would be expected. In addition, in the smaller UAS application, we apply a manufacturing constraint requiring linear distributions of blade geometry. In other words, we set blade geometry values at the root and tip of the blade and linearly interpolate between those to determine values at the various sections along the blade.

Our ducted acoustics model is limited to a combined tonal sound power level (SWL) at the duct inlet and outlet after decay of cut-off modes. In the context of aero-structural-acoustics of EDF for applications in this work, tonal sources are of greater concern in the rotor design than other noise sources. Specifically, perceived nuisance factors have been shown to be significantly more sensitive to tonal content than overall loudness [23]. This indicates that reducing tonal noise, even at the expense of some increase in broadband noise, can reduce the overall annoyance level associated with the EDF acoustics. In addition, experiments have shown for EDF that tonal noise tends to be greater than broadband noise for frequencies within human perception [24].

Despite the relative significance of tonal sources, we want to ensure that the optimizer does not take advantage of our acoustics model and select designs that have very large increases in broadband sources in order to meet our tonal SWL constraints. Without a ducted broadband acoustics model available, we employ a workaround procedure to ensure that the optimizer will not take advantage of our lack of broadband model. We use an open rotor Brooks-Burley [25] model³ to get a baseline value for open rotor broadband noise for initial optimizations run without any acoustics constraints. For subsequent constraints, where we progressively tighten the tonal SWL constraint, we also apply a constraint on the open rotor broadband, but only in the change from the unconstrained baseline. Specifically, we set the maximum allowable change in broadband OASPL to be no more than 6dB; which in isolation would nominally be just into the range of noticeably louder levels

³<https://github.com/OpenMDAO/AcousticAnalogies.jl>

for an open rotor.

By setting a limit on the allowed change in broadband OASPL, we ensure that the broadband level stays relatively constant, making sure the optimizer is not taking undue advantage. Furthermore, we will see in the results that rises in broadband approaching our limit happen alongside large increases in energy expense and are therefore undesirable designs in the first place.

3.2. Geometry and Geometric Design Variables

For the overall configuration, we start with rotor diameters of about 6 in for the UAS case and about 24 in for the two-seater case. We vary the duct chord length between 1.5 and 2.5 times the rotor radius in the studies in this work. Whatever the duct length, we place the rotor at the midpoint of the duct to allow a reasonable inlet length. We set the center body to begin aft of the duct leading edge at 75 percent the distance from the rotor plane to the duct leading edge. We extend the center body slightly aft of the duct trailing edge at a distance of $R_{tip}/3$. We maintain a constant rotor hub to tip ratio of 0.25 for the UAS case and 0.33 for the 2-seater case. Having a constant hub to tip ratio allows for significant levels of precomputation for our tonal acoustics model, making the optimization process more efficient. Figure 4 shows a meridional view of example duct and center body geometries with rotor actuator line location.

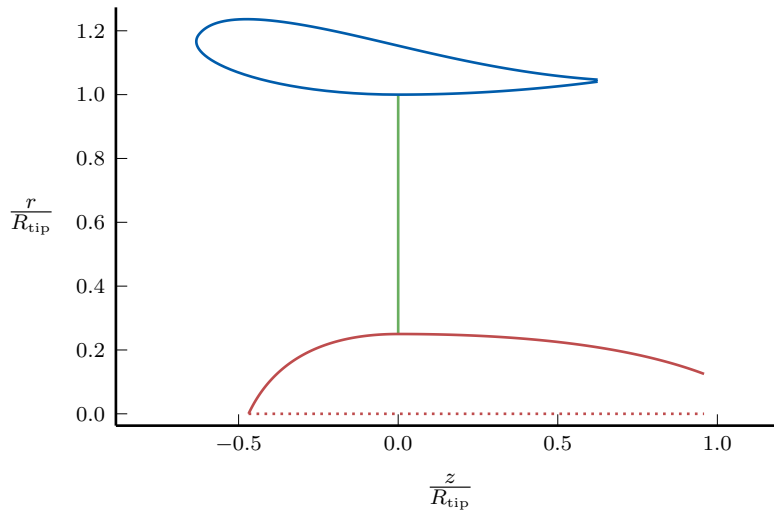
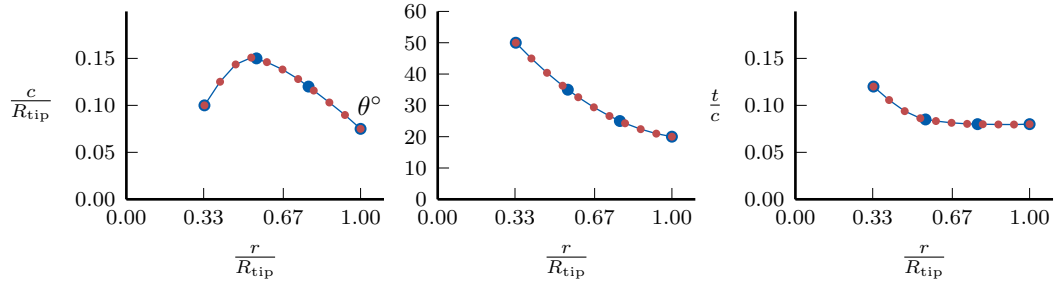


Figure 4: Meridional view of example geometry.

Rotor geometry design variables include chord and twist values along the blade as well as blade element thickness. To explore manufacturable designs for the small UAS case (2.25 in blades), we model linear blade distributions with two design variables each for chord, twist, and blade element thickness. In other words, the design variables control the root and tip geometries and intermediate locations are linearly interpolated. For the larger trainer case we add two additional design variables and define Akima [13] distributions for chord, twist, and thickness. For both applications, we pre-select 11 positions along the blade for blade sections and linearly interpolate between them to obtain the values for analysis. An example of the chord, twist, and thickness pre-selected positions from the Akima parameterization is shown in fig. 5.



(a) Example chord (c) parameterization. (b) Example twist (θ) parameterization. (c) Example thickness ratio (t/c) parameterization.

Figure 5: Visual explanation of the rotor geometry parameterization employed in this work. Blue circles indicate design variables, and smaller red circles indicate interpolated points for analysis.

For the duct and center body geometries, we generate the various surfaces using a composition of B-Spline curves. For the duct casing, we first define two quadratic B-Splines that meet at the center of the duct (where the rotor is placed). The first of these quadratic B-Splines is the green spline with square control points shown in fig. 6, and the second is the red spline with diamond control points. To define the specific casing geometry, we want a round leading edge and a sharp trailing edge. To get a round leading edge, we define an additional cubic B-Spline (see the other red spline with circle control points in fig. 6) that has three of the same control points as the front quadratic B-Spline (see the overlapping green square and red circle control points in fig. 6) The cubic spline includes one additional control point (the red circle

out in front in fig. 6) placed along the normal vector (represented by a dotted line) relative to the end of the quadratic spline. Using a cubic spline here gives us a round leading edge, rather than the corner seen between the green and blue lines in fig. 6. Placing the point along the normal vector results in the casing and nacelle surfaces to be tangent at the leading edge. The quadratic spline aft of the rotor (red with diamond control points) already results in a sharp trailing edge, so we use that for the back half of the casing geometry. We set the remaining control points of all of the B-Splines in such a way that the casing surfaces ahead of and behind the rotor smoothly connect at their junction (note all of the points along the dotted line at $r = R_{\text{tip}}$ in fig. 6).

To define the duct nacelle geometry, we use another cubic B-Spline (in blue in fig. 6). We place the first and second control points at the leading edge similar to how the casing spline points are positioned to ensure tangency at the leading edge. The distance of the second control points from the leading edge of the casing and nacelle inlet splines control the leading edge radius of the casing and is fixed for the optimizations in this work. We also place two additional control points whose radial positions ($N_{3,r}$ and $N_{4,r}$) provide suitable flexibility to the nacelle geometry.

Of the various parameters used to define the duct geometry, the following are selected as design variables. The radial position of the first control point of the splines defining the leading edge is a design variable that controls inlet area (see the tick labeled $I_{1,r}$ in fig. 6). Similarly, the radial position of the last control point of the splines defining the trailing edge is a design variable that controls the exit area (see tick labeled $O_{3,r}$ in fig. 6). The two control points whose radial positions ($N_{3,r}$ and $N_{4,r}$) control the nacelle geometry are also design variables.

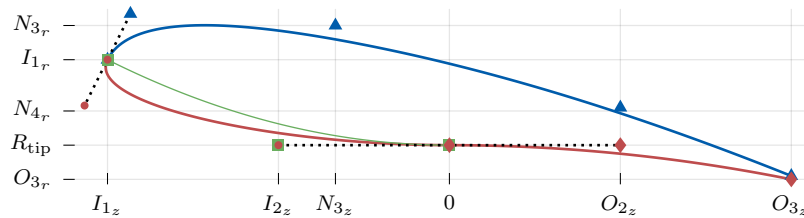


Figure 6: Visual explanation of the duct geometry parameterization employed in this work. Nacelle (blue) and casing (red) curves as well as front quadratic B-Spline (green). Black dotted lines indicate control points placed to enforce continuity.

Due to DuctAPE’s viscous drag model not being tightly coupled, it is helpful to apply some additional constraints to the duct geometry parameters to ensure a robust and feasible solution—avoiding difficult to model, viscous dominant, highly separated flow conditions. Specifically, we provide a minimum bound on the leading edge radius control point position (Note that this controls leading edge radius, but is not itself the value of the leading edge radius) of 0.15 and 0.05 times the duct chord length for the UAS and 2-seater cases, respectively. We also apply a maximum inlet radius constraint of 0.1725 times the duct length from the rotor tip radial position. In addition, we apply a minimum bound of 0.05 times the duct length above the rotor tip radial position to the radial position of penultimate nacelle control point that ensures a reasonable trailing edge wedge angle. For the 2-seater application, it was also helpful to add a constraint on the duct thickness to chord ratio to ensure a robust design that was not too thin. In that case we added a minimum 14 percent thickness ratio constraint.

3.3. Optimizer and Solver Settings

For the optimizations in this work, we use Sparse Nonlinear OPTimizer (SNOPT), a sequential quadratic programming algorithm for large-scale, constrained optimization [26]. To provide SNOPT with a Jacobian of the objective and constraint functions, we use ForwardDiff.jl, a Julia package for forward mode automatic differentiation [27].

4. Optimization Studies

4.1. Small UAS Propulsor Optimizations

4.1.1. Sweeping Acoustic Constraint

We begin the studies in this section with an exploration of the UAS application propulsor using a duct length of two times the rotor tip radius and a blade count of seven. We performed a sweep of acoustic constraints, beginning with an aero-structural optimization that does not constrain acoustics. From the acoustically unconstrained optimum we determined baseline values for tonal and broadband sources. We then ran optimizations at incrementally decreasing tonal sound power level (SWL) constraints until we could no longer find a feasible solution given our various aero-structural-acoustic constraints. From the results, we can grasp the fundamental aerodynamic-structural-acoustic interactions taking place as we make more stringent acoustic requirements.

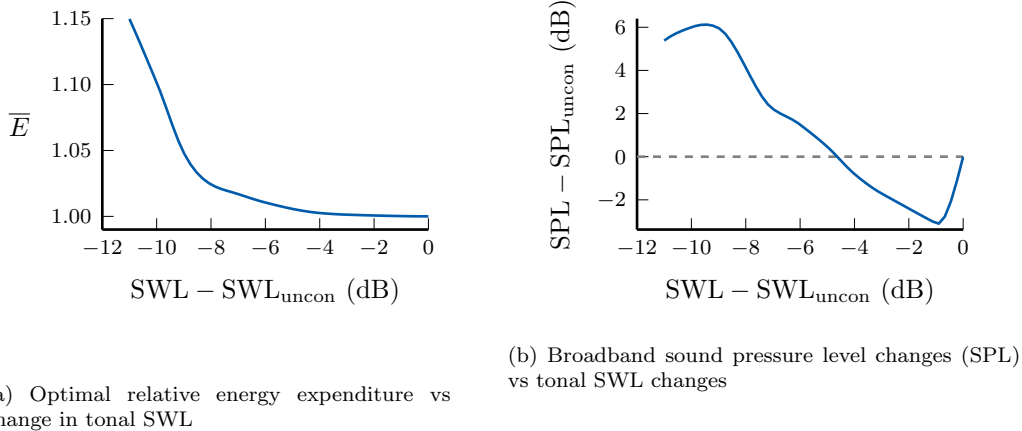
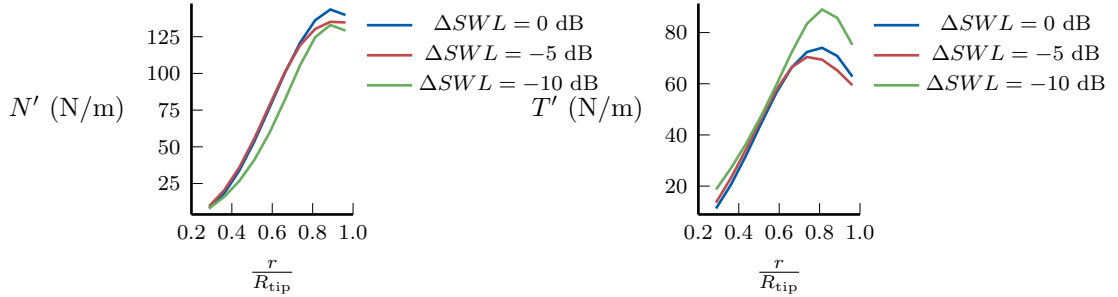


Figure 7: UAS case energy and broadband sound pressure level vs tonal sound power level for a blade count of seven and a duct length of $2R_{\text{tip}}$.

Figure 7 shows the relative change in optimal energy and broadband sound pressure level (SPL) as the tonal SWL constraint is decreased relative to the acoustically unconstrained sound power level. Focusing first on fig. 7a we see that until about -5 dB, there is less than a 1 percent change in energy expense. (Note that this is very similar to results seen in the high-fidelity studies by Jaron et al. as mentioned in section 1.) After 5 dB, we start to see energy expense increase, and then after 8 dB or so, we see a relatively sharp increase until a feasible design can no longer be achieved. Comparing the energy expense to the changes in broadband in fig. 7b we see that in this case the larger increases in energy expense coincide with increases in broadband noise above the initial unconstrained value. This lends confidence to our workaround approach to model broadband noise as we explore the effects of tonal noise constraints on the ducted rotor system.

Figure 8 can help us to begin unpacking the various aero-structural-acoustic trade-offs as we reduce the tonal SWL constraint. Figure 8 shows the normal (N') and tangential (T') blade loading distributions for the static operating point at each end of the feasible range for tonal SWL as well as the midpoint of that range. From the unconstrained case to a 5 dB decrease (blue to red curves), the approach to meet the tonal SWL constraint appears to be a shifting of the loading away from the tip. We see a decrease in normal and tangential loading toward the tip, with very slight increases across the rest of the blade. This reduces the biggest contributors to tonal SWL



(a) Blade normal loading per unit span

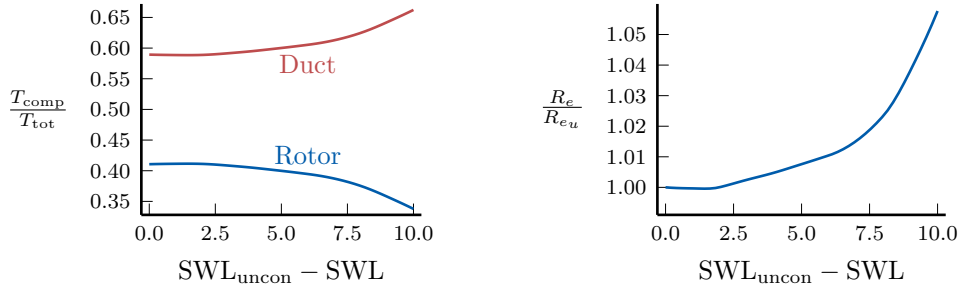
(b) Blade tangential loading per unit span

Figure 8: A comparison of the blade loading for the static operating point shows that as the acoustic constraint becomes more stringent, the optimizer seeks different ways to reduce the loading sources of noise while still meeting the thrust constraints.

as modeled in this work, thereby allowing the optimizer to meet the SWL constraints initially.

The small magnitudes of those initial changes lead to the relatively small magnitude of change in required energy. On the other hand, after a 5 dB decrease in the SWL constraint, we can see how the tangential loading goes up significantly. Since the tangential loading defines torque and is a major component of rotor power, the large increase in tangential loading is directly related to the large increase in energy expense seen in fig. 7. At the same time, we see a similarly significant decrease in normal loading across the blade. Since blade normal loading directly determines rotor thrust, we therefore have a reduction in rotor thrust as the SWL constraint is reduced. The reductions in normal loading seen in fig. 8a highlight one of the advantages of using ducted fans for quiet propulsion systems.

Despite the reduction in rotor thrust, the required thrust constraints are active in all of these optimizations. As the acoustic constraint is reduced, the optimizer selects designs that reduce rotor contribution to thrust in the static case. As we can see in fig. 9, as the relative contribution of the rotor thrust decreases we also see an increase in the duct contribution (see fig. 9a). This increase in duct induced thrust is driven by the optimizer selecting designs with increased duct exit area (see fig. 9b). With the increase in duct-induced thrust, the static thrust constraint can be met even as the rotor contribution to thrust decreases to meet acoustic constraints. In this way, ducted rotors



(a) Body and rotor thrust contributions vs ΔSWL (b) Change in relative duct radius (relative to acoustically unconstrained radius, R_{e_u}) vs ΔSWL

Figure 9: Relative contributions (T_{comp}) of body and rotor to total (T_{tot}) static thrust for the seven blade case shows that indeed the rotor contribution decreases as the acoustic constraint drops, but an increasing exit area allows body-induced thrust to compensate to meet thrust requirements.

exhibit additional advantage over open rotor systems due to the increased flexibility in approaches to reduce tonal noise sources.

Let us now look into even more details regarding the aero-structural-acoustic trade-offs in these optimizations. For the most part, this optimization problem is dense, with most inputs affecting most of the constraints (the exception being the rotation rate only affecting constraints for the same operating points). Since our tonal acoustics model is based on lift and thickness sources, the two major aspects of the design the optimizer can change to meet stricter acoustic constraints are the blade thickness distribution and the blade loading distribution. The blade loading distributions is a function of the chord, twist, thickness, and rotation rate. The detailed trade-offs come about due to the aerodynamic and structural behavior of the system also being determined by the chord, twist, thickness, and rotation rate. In the structural case, we are also concerned with the blade loading and ensuring that the thickness and chord lengths are sufficiently large to meet the structural and manufacturing constraints. At the same time, the optimizer is attempting to drive the aerodynamics to the most efficient design for a given thrust constraint in order to minimize energy.

Figure 10 shows the optimal blade geometries at the same SWL constraints we have been exploring thus far. For the optimal baseline design (see the blue lines in fig. 10), the active constraints include all of the operating point thrust constraints, the tip thickness constraint, and the root

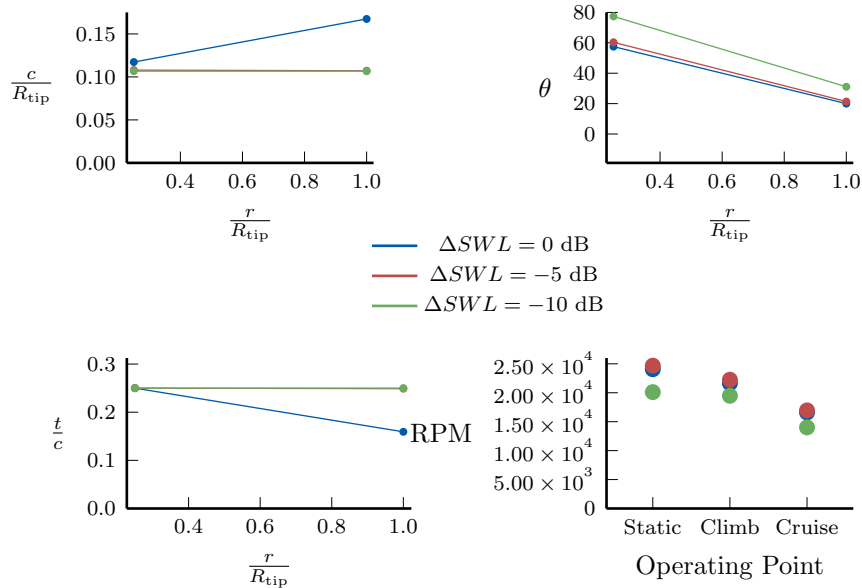


Figure 10: Rotor designs for a linear blade as the tonal SWL is reduced from unconstrained to -10 dB.

structural failure constraint in the static condition. If we were to relax the minimum thickness we could potentially see a tip displacement constraint become active rather than the root failure constraint; but that would require impractically thin blades.

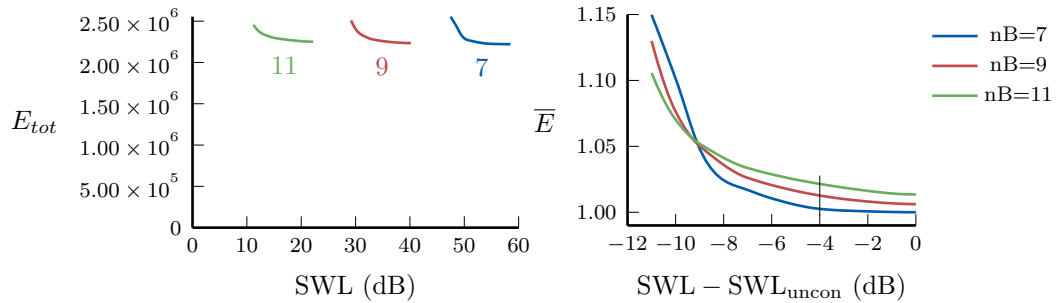
As we require reduced SWL levels, the root chord and thickness stay relatively constant to meet the structural failure criteria in the static condition. Initially, the tip chord drops to help shift the blade loading away from the tip. With a drop in chord, a slight increase in the rotation rate and twist is required to meet thrust constraints. Since the minimum thickness constraint is active at the blade tip, we also require an initial increase in the thickness ratio at the blade tip to continue meeting the thickness constraint.

After 5 dB, the thickness constraint and maximum thickness ratio bound become active across the entire blade. In order to continue meeting tonal SWL constraints without being able to adjust the chord or thickness ratio, the optimizer finds the only option is to reduce the rotation rate. With the reduced rotation rate, an increase in twist is required to meet thrust constraints. This combination of decreased rotation rate and increased twist

is what drives the large increase in tangential loading. And as we have already discussed, the increased tangential loading leads to the quick rise in energy expense as we require more stringent SWL levels.

To highlight some of the aspects of acoustic trade-offs we see here, the optimizer finds it advantageous to reduce chord in order to find a quieter design. As noted, this gain in quieter tonal SWL comes at the expense of increased thickness, which is also a source of tonal SWL in our model. It is obvious from these results, however, that the overall SWL value is more sensitive to the loading sources than the thickness sources. On the other hand, it is the combination of larger thickness ratios and high angles of attack that increase the broadband noise, so there are additional, detailed, acoustic trades to be considered in future work.

4.1.2. Sweeping Blade Count



(a) Optimal energy expenditure vs sound power level (b) Optimal relative energy expenditure vs change in sound power level

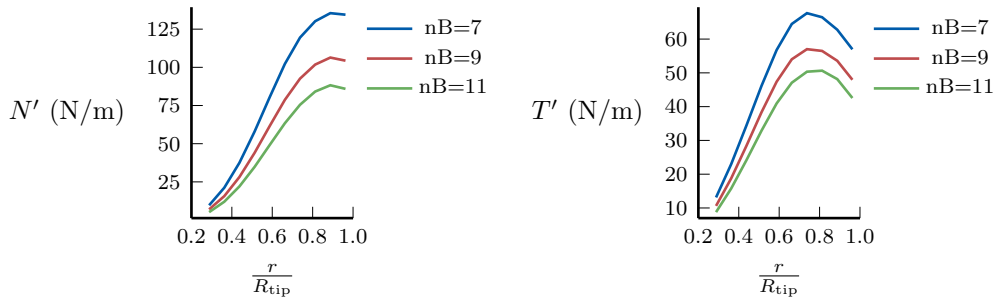
Figure 11: UAS case Pareto front across various numbers of blades at a duct length of $2R_{tip}$.

As we look at other blade counts, we find that each has a band of feasible SWL, though the bands are shifted lower as blade count increases. In fig. 11 we see the Pareto front of energy expenditure vs SWL for the case just presented (the blue curve for seven blades) as well as for nine and 11 blades. Figure 11a shows the total energy (E_{tot}) vs the SWL constraint values for each optimization. Figure 11b shows the energy (\bar{E}) relative to the seven blade baseline energy value plotted against the change in SWL from each configuration's baseline SWL. In both plots, the right side of each curve

is the energy and associated SWL value resulting from the aero-structural optimization of each configuration with unconstrained acoustics. The left side of each curve is defined by a feasibility limit where we can no longer decrease the tonal SWL while meeting the other constraints.

Similar to the seven blade case, in the nine and 11 blade configurations we can generally get about a 5 dB decrease with less than a 1 percent change in the energy expense. As we require lower tonal SWL magnitudes, however, the optimizer has no choice but to deviate from more efficient designs. This deviation then leads to the rapid increase in energy expense as we approach feasibility limits. On the other hand, achieving the same reduction in tonal SWL appears to be as simple as adding additional blades.

For each configuration, we can achieve a total reduction in SWL of roughly 10 dB; similarly, we can achieve roughly a 10 dB reduction in SWL by simply adding a single blade. Figure 11b shows, however, that increasing blade count comes at an increased energy cost. At the acoustically unconstrained optima, there is a roughly 0.61 percent increase from seven to nine blades and a 1.5 percent increase from seven to 11 blades. As we can see in fig. 11b, this difference increases for reasonable reductions in SWL under the assumptions and constraints of this study.



(a) Blade normal loading per unit span

(b) Blade tangential loading per unit span

Figure 12: As the blade count increases, the blade loading at a given relative acoustic constraint (in this case 4 dB below the unconstrained value for each blade count) decreases for individual blades.

Figure 12 shows the blade loadings at seven, nine, and 11 blades for designs constrained at 4 dB below their respective unconstrained acoustic designs (see the black tick in fig. 11b). Despite decreasing loading, we see di-

minishing returns in load reduction as blade count increases, indicating that some part of the design is unable to acoustically take full advantage of the higher blade counts. With more blades, the optimizer wants to reduce the chord lengths in order to have similar efficiencies across blade counts. With these small blades however, the higher blade counts run into the minimum thickness constraint and the thickness ratio upper bound quite quickly. In fact, for the nine and 11 blade cases here, the root failure constraint is inactive, but both root and tip thickness constraints are active. Therefore, with more blades the rotors must have higher solidities (σ) in order to meet the minimum thickness manufacturing constraints.

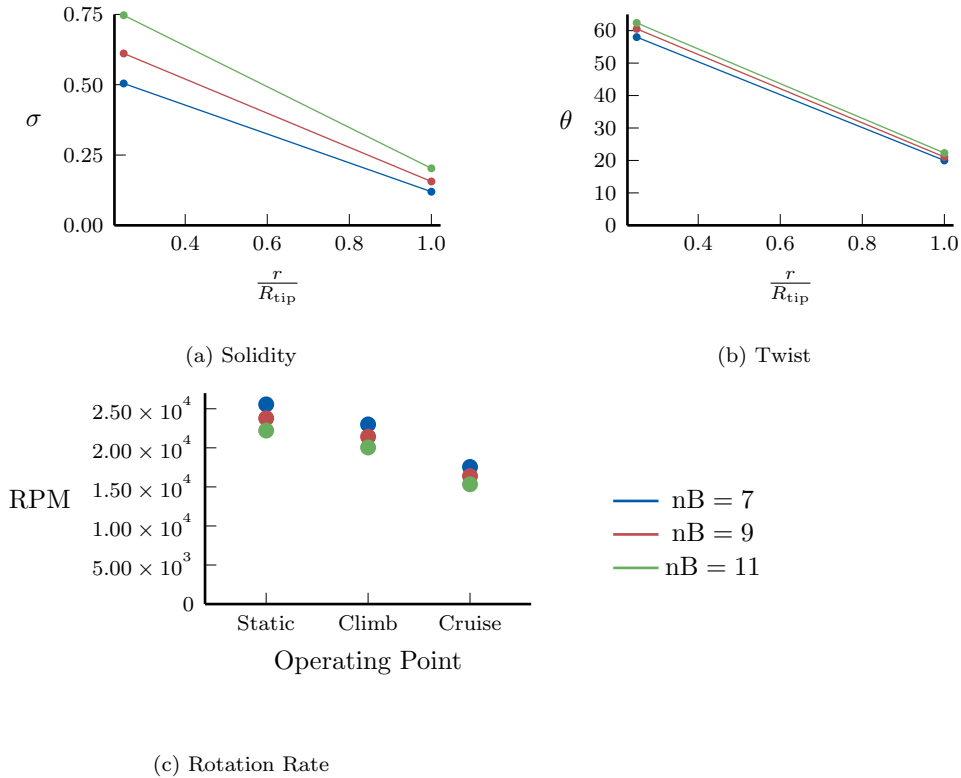


Figure 13: Rotor designs at blade counts of seven, nine, and 11, all at sound power levels 4 dB below the unconstrained value for each case.

We can see these geometry details in fig. 13, which shows the rotor solidity, twist, and rotation rate for seven, nine, and 11 blades each at a SWL 4 dB below their respective unconstrained SWLs. The higher solidity for

larger blade counts forces a reduction in rotation rate and increase in blade twist in an ineffectual effort to get the same energy expense as lower blade counts. Thus we see an increase in the energy required for more blades in this application, despite the optimizer maximizing efficiency within the applied constraints.

4.1.3. Sweeping Duct Length

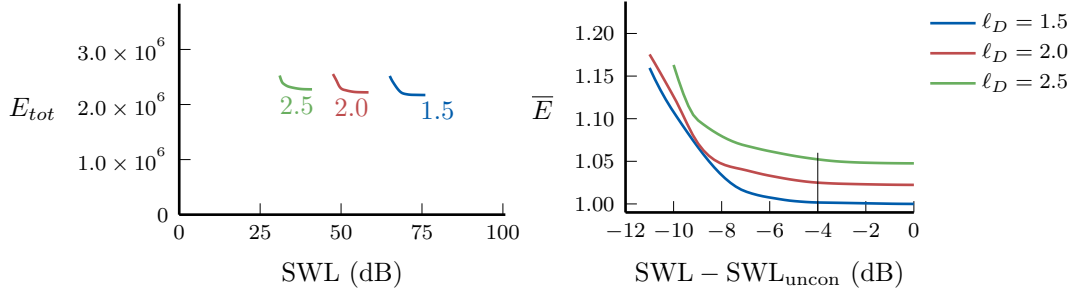
Another approach to easily reduce EDF noise is to lengthen the duct. Based on the discussion of cut-off modes in section 2.4, we know that a longer duct will help decay the acoustic cut-off modes, leading to a quieter design. Figure 14 shows the energy vs SWL constraint for duct lengths between $1.5R_{tip}$ and $2.5R_{tip}$. Figure 14a compares the total energy vs SWL constraint values. Figure 14b compares the energy relative to the acoustically unconstrained energy for the $1.5R_{tip}$ configuration with the change in SWL constraint from each configuration's respective unconstrained SWL value.

For a given configuration we again see that initial decreases in tonal SWL do not require much increase in energy. In addition, the rise in energy happens earlier for increased duct length rather than later as we saw for increased blade count. Similar to the relatively large jumps in SWL ranges for differences in blade counts, we see here how a relatively small change in duct length can lead to significant reductions in SWL. In this case, we see a roughly 40 dB change for a change in duct length equal to one rotor tip radius. Interestingly, it appears that the decrease in SWL with increasing duct length is almost entirely a product of the duct decaying the acoustic cut-off modes.

Table 4: The lack of difference in rotor design between duct lengths of 1.5 and 2.5 times rotor tip radius with acoustic constraints 4dB below the nominal acoustic level for each duct length indicates that duct length is nearly solely responsible for the variation in sound power level seen in fig. 14.

Duct Length	Solidity (σ)	Twist (θ)	Thickness Ratio (t/c)	RPM
$1.5R_{tip}$	[0.515, 0.125]	[54.9, 20.0]	[0.25, 0.238]	[25854.0, 23052.0, 17648.0]
$2.0R_{tip}$	[0.504, 0.12]	[58.0, 20.0]	[0.25, 0.248]	[25559.0, 22994.0, 17553.0]
$2.5R_{tip}$	[0.483, 0.124]	[61.9, 20.8]	[0.25, 0.24]	[24553.0, 22263.0, 16934.0]

Table 4 shows values for the rotor design variables for three different



(a) Optimal relative energy expenditure vs sound power level (b) Optimal relative energy expenditure vs change in sound power level

Figure 14: UAS case energy vs sound power level across a series of duct lengths at a blade count of 7.

duct lengths (1.5, 2.0, and 2.5 times the rotor tip radius) all at the same relative acoustic constraint. Specifically, these designs are all at 4 dB below the unconstrained SWL for the given duct length (see the black vertical tick in fig. 14b). We see that despite spanning a nearly 40 dB range, for the same relative acoustic value the rotor geometry is the nearly same; and thus the changes in SWL shown in fig. 14 are almost entirely a function of duct length. Another benefit of a longer duct is a longer inlet area to align flow, which can be beneficial for non-axisymmetric flows. On the other hand, a longer duct is both heavier and results in higher drag, which increases the energy consumption as shown in fig. 14b. Specifically, we have a 2.2 percent increase when increasing duct length from $1.5R_{tip}$ to $2.0R_{tip}$, and a 4.8 percent increase from $1.5R_{tip}$ to $2.5R_{tip}$.

4.2. 2-Seater Propulsor Optimizations

We now look at the larger propulsor for the 2-seater application based on the Airbus E-Fan demonstrator. As mentioned, we used two additional design variables each for chord, twist, and thickness along the blades in this study rather than linear blades like the UAS application. While linear blades do provide benefits in manufacturability, allowing the optimizer additional flexibility can help us see in more detail the aero-structural-acoustic trades as we tighten the tonal SWL constraints. In addition for this application, we applied a rotor tip Mach constraint of 0.5 to keep the blade element aerodynamics within the underlying assumptions of the DuctAPE solver.

4.2.1. Sweeping Acoustic Constraint

We will begin again looking at a single configuration across a range of acoustic constraints. In this case, we look at a nine blade case with a duct length 2.25 times the rotor tip radius. In fig. 15 we see the normal and tangential loading for the static case across several SWL constraints. Just as with the UAS application, to meet the acoustic constraint, the optimizer selects designs that reduce the rotor tip loading, de-loading the rotor’s responsibility for thrust in the static case. In addition, we see a similar reduction in tangential loading for this static loading case. At first glance we might question why the tangential load initially decreases as that could potentially lead to a more efficient design than was found in the acoustically unconstrained case. This may be true for the static component being plotted, but the overall combined effect of the changes in loading and rotation rate across static, climb, and cruise operating points results in an overall increase in energy expense.

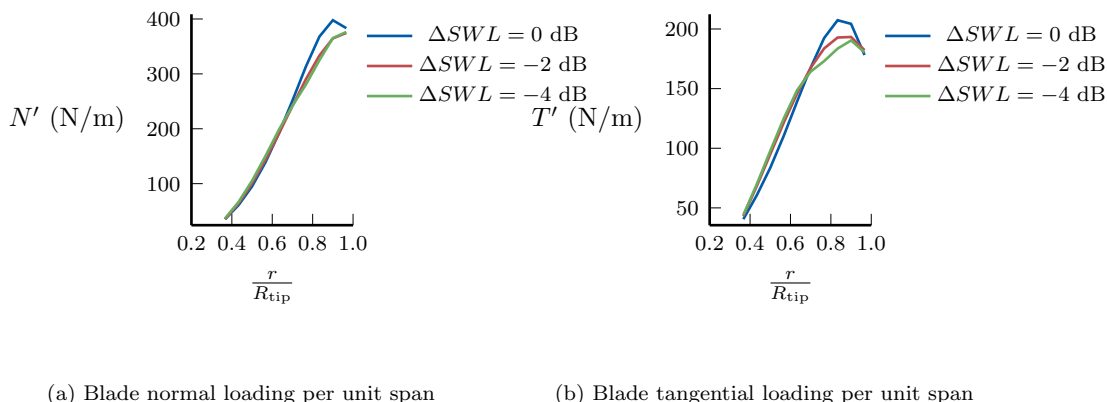


Figure 15: In the two-seater case loading, we again see the general strategy for reducing tonal noise is to focus on decreasing loading toward the tip.

We can see the trade in energy vs SWL constraint in fig. 16a, which shows the relative changes in the components of energy associated with each of the flight mission operation points. We first notice that the relative energy in the static condition does indeed go down as the duct exit opens up and takes some of the burden of the static condition thrust. This allows the normal loading on the rotor blades to drop while still meeting thrust constraints. With the integrated tangential loading (torque) going down as well (see fig. 16b), the total power in the static condition decreases. In contrast, the climb operating

point is less affected, with a slight increase in torque; meanwhile the cruise energy and torque noticeably increase as the duct geometry becomes more inefficient for cruise conditions. Since the total energy is dominated by the longer times in climb and cruise, we see an overall rise in energy despite apparent benefits to the static aerodynamics with decreased static condition SWL (see the dashed black line in fig. 16a).

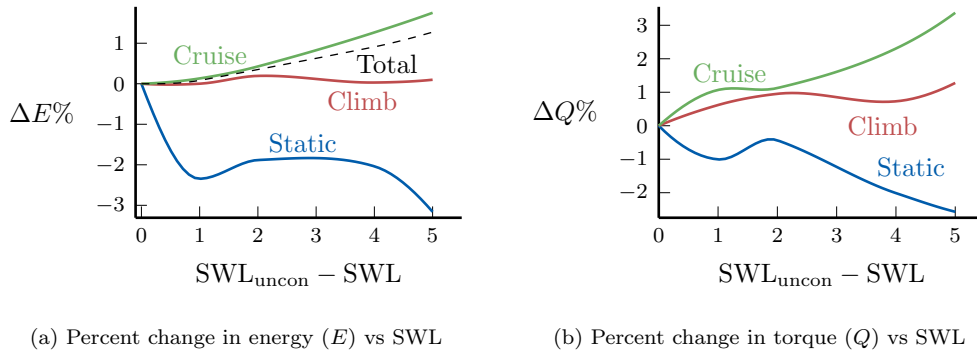


Figure 16: We can see comparing torque and energy that despite the torque and energy decreasing for the static condition, the cruise condition dominates and leads to an overall rise in energy expenditure as the tonal SWL constraint is tightened.

Figure 17 shows the rotor designs ranging from unconstrained to 4 dB below the baseline SWL values. We can see here the effort of the optimizer to shift the loading root-ward in an effort to meet the tighter acoustic constraints. As the loading shifts root-ward, the root bending moment for the -2 dB constraint is reduced; which allows the root thickness to be reduced while still meeting structural criteria. As we continue to decrease the tonal SWL constraint to -4 dB, however, a slightly higher static operating point RPM is required to meet thrust constraints as the chord lengths are reduced to meet the acoustic constraint. With reduced chord and increased rotation rate, a slightly higher root thickness ratio is required to meet structural constraints (note that the root section failure constraint is active in each of these optimizations). At the same time, the reduced chord lengths across the blade require increased thickness ratios to meet the minimum thickness constraint.

We also see the main mechanisms of broadband increase in fig. 17. Specifically in the -4 dB case, the chord is reduced along the outer half of the blade, requiring an increase of thickness to meet the minimum thickness constraint. The thicker section results in lower local lift, requiring an increase in the twist in that region to meet the thrust constraint. The increased thickness

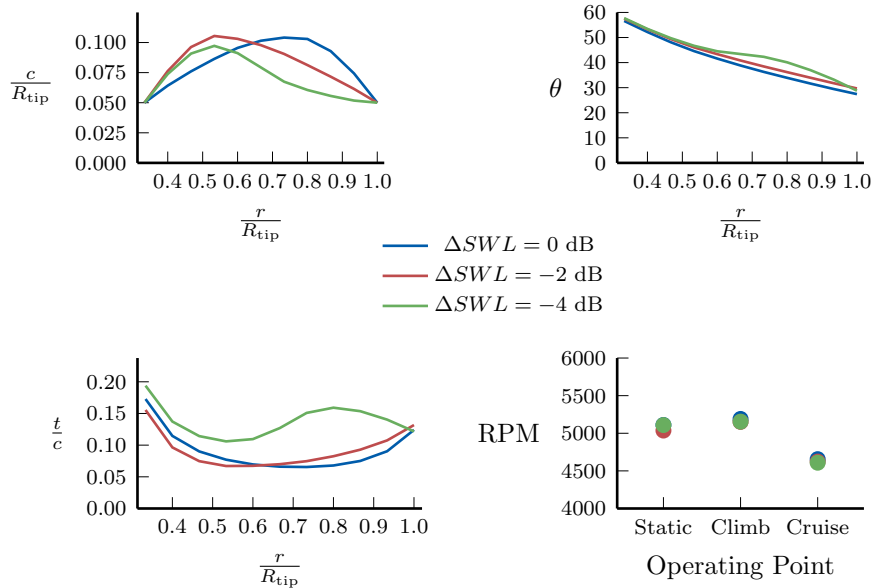


Figure 17: The more flexible rotor design more clearly shows the efforts of the optimizer to shift the geometry in such a way to move loading root-ward as tighter SWL constraints are required.

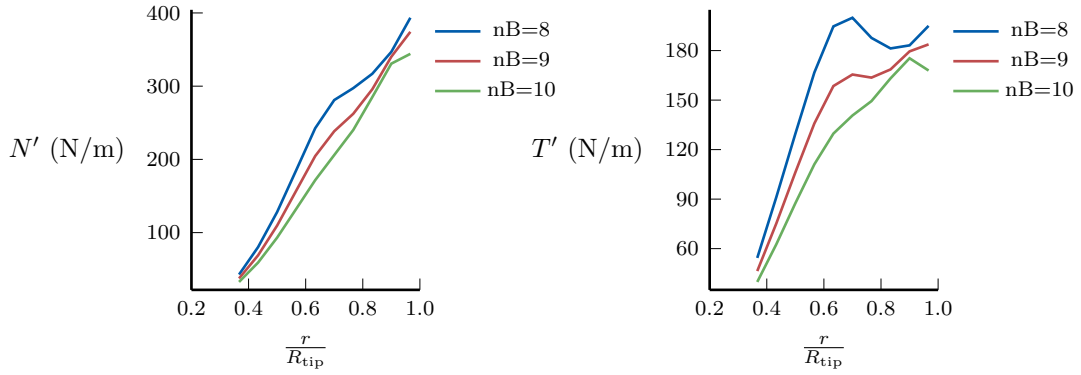
and angle of attack are both mechanisms that increase the broadband level. These effects show us why increases in energy expenditure are accompanied by increases in broadband noise as modeled in this work.

4.2.2. Differences with Blade Count

We next look at various blade counts. Even with the larger blades in this case, the relative contribution of the rotor weight is even smaller than for the UAS case, meaning energy increases due to blade count are aerodynamic in nature. The blade loading across various blade counts shown in fig. 18 resembles what we saw in the UAS case, but with larger magnitudes for the larger thrust requirements. So again, we have a roughly 10 dB decrease in tonal SWL with each blade added.

In contrast to the UAS case, the more flexible parameterization allows for an overall reduction of solidity across the blade as seen in fig. 19. This general reduction is also accompanied by a slightly increased root solidity and an increased thickness across most of the blade. This indicates that there is indeed an aerostructural trade to be had, as it is aerodynamically

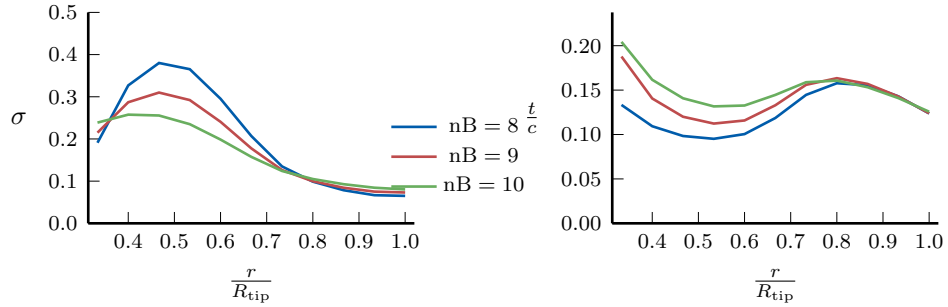
advantageous to reduce solidity. On the other hand, some level of thickness is required to meet the structural constraints, so the section thickness ratio must be increased if chord is reduced. An increased thickness ratio also happens to be detrimental to both the aerodynamics and acoustics, but is obviously less detrimental than the gains in solidity reduction.



(a) Blade normal loading per unit span

(b) Blade tangential loading per unit span

Figure 18: As the blade count increases, the blade loading at a given relative acoustic constraint (in this case 5 dB below the unconstrained value for each blade count) decreases for individual blades.



(a) Solidity

(b) Thickness Ratio

Figure 19: Solidity and thickness ratio at blade counts of eight, nine, and ten, all at sound power levels 5 dB below the unconstrained value for each case.

4.3. Comparing Duct Geometries

The optimizer took different approaches to duct design for each of these applications. Remember the UAS is small, has a shorter relative cruise time, and a higher relative loading requirement in static conditions. On the other hand, the 2-seater case is largely dominated by time in cruise. These differences are reflected in the duct shapes.

Figure 20 shows the baseline (unconstrained acoustics) geometries. We can see that the UAS case favors a geometry more suitable for static conditions, or at least thrust at lower speeds. The exit is relatively more open—causing the duct induce more thrust, and the inlet opens up in order to position the stagnation points well for cruise and climb. In comparison, the 2-seater geometry is more closed leading to reduced drag in climb and cruise conditions.

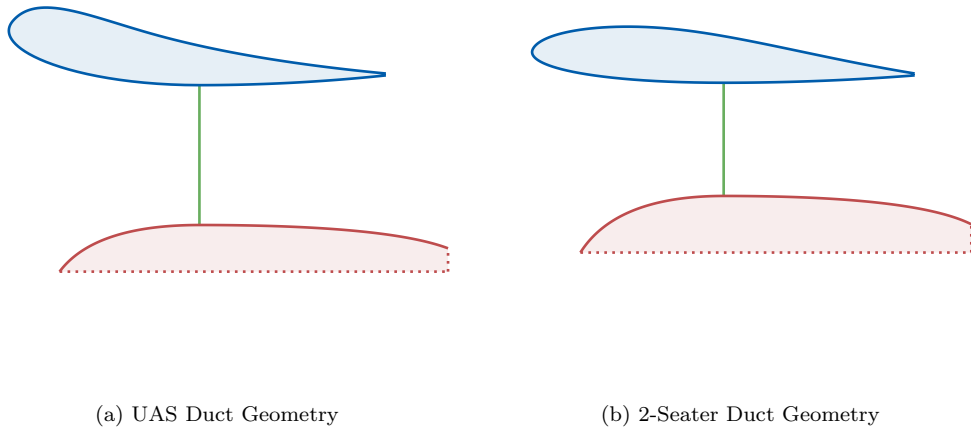


Figure 20: Comparison of the normalized duct geometries for the unconstrained acoustic cases.

Before getting too far into fine details, we remind the reader that in both cases we applied some constraints on the duct geometries to avoid separated flow conditions that DuctAPE is incapable of modeling (see the end of section 3.2 for specific values). Specifically, we set a minimum bound on the leading edge radius control, which needed to be slightly larger for the UAS case as it had a larger inlet opening and more drastic nacelle curvature. In addition, we applied a minimum bound on the penultimate nacelle control point in both cases, but this constraint was only active for the UAS case.

We also applied a maximum inlet radius to the UAS case since the optimizer was driving into spaces with very open designs leading to massive separation that DuctAPE was incapable of modeling. Finally, we set a constraint on minimum thickness to chord ratio for the 2-seater duct to ensure the design would be relatively robust to non-axial freestream conditions we are unable to model.

With all of that said, the geometries generally remain unchanged from those shown in fig. 20 as acoustic constraints are applied. The exception being the exit areas which we have already shown to increase with tighter tonal SWL constraints. In the 2-seater case, the inlet also opens just barely as the exit opens up as well, but it never hits the upper bound the UAS case started at in the acoustically unconstrained optimization. The relative lack of change in duct geometry makes sense as the most direct effect the duct has on the acoustics is to cut off specific acoustic modes. Even with relatively small changes in duct geometry, the presence of the duct allows the rotor design more flexibility to meet acoustic constraints. These acoustic benefits due to the presence of a duct serve to highlight some of the reasons behind the interest in using EDF technology in advanced air mobility applications.

5. Conclusion

In this work, we have applied an axisymmetric, ducted fan aerodynamic analysis code: DuctAPE along with a Geometrically eXact Beam model, GXBeam, and a tool for determining the in-duct tonal sound power levels for electric ducted rotors in order to perform aero-structural-acoustic optimization. We explored two applications: a small generic UAS, and a larger 2-seat airplane based on the Airbus E-Fan demonstrator. In both cases, we saw that for a given configuration (duct length and blade count) there was a band of feasible tonal sound power levels. The feasible tonal sound power levels extend from the acoustic levels of the aero-structural optimum until an optimal solution meeting all aero-structural-acoustic requirements could no longer be achieved.

In exploring these feasible ranges of tonal sound power levels, we found several trends to be consistent across the range of sizes and loading explored for the low-Mach applications in this work. For changes in blade count, we generally saw a 10 dB reduction in the feasible tonal sound power level as modeled in this work for each blade added. For changes in duct length,

we saw a roughly 40dB reduction in feasible tonal sound power levels for a change in duct length of $1.0R_{tip}$.

On a detailed blade design level we saw that the general strategy for reducing tonal sound power level was to shift the blade loading distribution away from the blade tip. This shifting had the effect of reducing the rotor thrust and increasing the duct-induced thrust. The increase in duct-induced thrust was accomplished by increasing the duct exit area. Although allowing for a quieter design and more efficiency in the static operating point, the increased duct exit area was less efficient for climb and cruise and led to overall increases in energy expenditure as the tonal sound power level was decreased.

For acoustic constraints within 4 dB of the acoustically unconstrained baseline values, we generally saw no more than a 1 percent increase in required energy expenditure. As the tonal sound power level constraint was further reduced, we saw that the tangential blade loading increased aggressively as greater torque was required at reduced rotation rate. This increase in tangential loading increased the torque and therefore power and energy despite the reduction in rotation rate. We generally saw increases in energy expenditure of roughly 15 percent before reaching feasibility limits within our applied constraints.

In future work, we recommend refining the acoustics models through the development and implementation of a broadband model applicable to ducted fans and suitable for gradient-based optimization. We also recommend adding stator design to the optimizations with associated additions to the acoustic model to capture blade-stator interaction cut-off modes. Additional disciplines would also help to build a system/mission-centric optimization framework; some initial ideas include a motor/battery or other power train model as well as a thermal management model for larger propulsors. Other interesting applications could also involve systems combining open and ducted propulsors and other novel preliminary design projects.

6. Acknowledgments

This paper is based upon work supported by NASA under award No. 80NSSC23M0218.

References

- [1] K. Antcliff, N. Borer, S. Sartorius, P. Saleh, R. Rose, M. Gariel, J. Oldham, C. Courtin, M. Bradley, S. Roy, B. Lynch, A. Guiang, P. Stith, D. Sun, S. Ying, M. Patterson, V. Schultz, R. Ganzarski, K. Noertker, C. Combs, R. Ouellette, Regional Air Mobility: Leveraging Our National Investments to Energize the American Travel Experience, Technical Report, NASA, 2021.
- [2] . Koppelberg, D. Weintraub, P. Jeschke, Acoustic pre-design studies of ducted fans for small aircraft, *CEAS Aeronautical Journal* 13 (2022) 877–889.
- [3] J. Qing, Y. Hu, Y. Wang, Z. Liu, X. Fu, W. Liu, Kriging Assisted Integrated Rotor-Duct Optimization for Ducted Fan in Hover, in: *AIAA Scitech 2019 Forum*, American Institute of Aeronautics and Astronautics, San Diego, California, 2019. doi:10.2514/6.2019-0007.
- [4] R. Jaron, A. Moreau, S. Gu erin, L. Enghardt, T. Lengyel-Kampmann, T. Otten, E. Nicke, Multidisciplinary design optimization of a low-noise and efficient next-generation aero-engine fan, *Journal of Turbomachinery* 144 (2021) 011004.
- [5] J.-H. Kim, B. Ovgor, K.-H. Cha, J.-H. Kim, S. Lee, K.-Y. Kim, Optimization of the aerodynamic and aeroacoustic performance of an axial-flow fan, *AIAA Journal* 52 (2014) 2032–2044.
- [6] G. Grasso, S. Moreau, J. Christophe, C. Schram, Multi-disciplinary optimization of a contra-rotating fan, *International Journal of Aeroacoustics* 17 (2018) 655–686.
- [7] S. Qiu, A continuous adjoint-based aeroacoustic shape optimization for multi-mode duct acoustics, *Proceedings of the Institution of Mechanical Engineers, Part C: Journal of Mechanical Engineering Science* 232 (2018) 3897–3914.
- [8] M. Biava, G. N. Barakos, Optimisation of ducted propellers for hybrid air vehicles using high-fidelity cfd, *The Aeronautical Journal* 120 (2016) 1632–1657.

- [9] T. Zhang, G. N. Barakos, High-fidelity numerical investigation of ducted propeller aerodynamics/acoustics and adjoint-based design optimisation, 77th Vertical Flight Society (VFS) Annual Forum (2021).
- [10] J. Bezanson, A. Edelman, S. Karpinski, V. B. Shah, Julia: A fresh approach to numerical computing, *SIAM Review* 59 (2017) 65–98.
- [11] J. Mehr, A. Ning, Ductape: A steady-state, axisymmetric ducted fan analysis code designed for gradient-based optimization., in: *AIAA Aviation Forum, Las Vegas, 2024*. doi:10.2514/6.2024-4297.
- [12] J. Mehr, N. Lehnhof, A. Ning, Ductape: A steady-state, axisymmetric ducted fan analysis code designed for gradient-based optimization., *In Review* (2025).
- [13] H. Akima, A new method of interpolation and smooth curve fitting based on local procedures, *Journal of the Association for Computing Machinery* 17 (1970) 589–602.
- [14] W. Yu, M. Blair, Gebt: A general-purpose nonlinear analysis tool for composite beams, *Composite Structures* 94 (2012) 2677–2689.
- [15] Q. Wang, W. Yu, Geometrically nonlinear analysis of composite beams using wiener-milenković parameters, *Journal of Renewable and Sustainable Energy* 9 (2017) 033306.
- [16] T. McDonnell, A. Ning, Gxbeam: A pure julia implementation of geometrically exact beam theory, *Journal of Open Source Software* 7 (2022) 3997.
- [17] T. McDonnell, A. Ning, Geometrically exact beam theory for gradient-based optimization, *Computers & Structures* 298 (2024).
- [18] T. Critchfield, A. Ning, Mission-focused multidisciplinary design optimization of tilt-rotor evtol propulsion system, *Journal of Aircraft* (In Review) (2025).
- [19] V. Giavotto, M. Borri, P. Mantegazza, G. Ghiringhelli, V. Carmaschi, G. Maffioli, F. Mussi, Anisotropic beam theory and applications, *Computers & Structures* 16 (1983) 403–413.

- [20] M. Goldstein, *Aeroacoustics*, Advanced book program, McGraw-Hill International Book Company, 1976.
- [21] J. E. F. Williams, D. L. Hawkings, Sound generation by turbulence and surfaces in arbitrary motion, *Philosophical Transactions of the Royal Society of London. Series A, Mathematical and Physical Sciences* 264 (1969) 321–342.
- [22] A. Moreau, *A Unified Analytical Approach for the Acoustic Conceptual Design of Fans of Modern Aero-Engines*, Ph.D. thesis, Technische Universität Berlin, 2016.
- [23] R. Merino-Martinez, S. Schade, Psychoacoustic analysis of the perceptual influence of rotational speed fluctuations in an urban mobility vehicle with distributed ducted fans, in: *54th International Congress & Exposition on Noise Control Engineering*, 2025.
- [24] A. Truong, D. Papamoschou, Harmonic and broadband separation of noise from a small ducted fan, in: *21st AIAA/CEAS Aeroacoustics Conference*, 2015. doi:10.2514/6.2015-3282.
- [25] T. Brooks, C. Burley, Rotor broadband noise prediction with comparison to model data, in: *7th AIAA/CEAS Aeroacoustics Conference and Exhibit*, 2001. doi:10.2514/6.2001-2210.
- [26] P. E. Gill, W. Murray, M. A. Saunders, SNOPT: An SQP Algorithm for Large-Scale Constrained Optimization, *SIAM Journal on Optimization* 12 (2002) 979–1006.
- [27] J. Revels, M. Lubin, T. Papamarkou, Forward-mode automatic differentiation in Julia, arXiv:1607.07892 [cs.MS] (2016).